Check for updates

# Hybrid Multifluid Algorithms Based on the Path-Conservative Central-Upwind Scheme

**Alina Chertock[1] · Shaoshuai Chu[2] · Alexander Kurganov[3]**

© The Author(s), under exclusive licence to Springer Science+Business Media, LLC, part of Springer Nature 2021

## Abstract
We develop new hybrid numerical algorithms for compressible multicomponent fluids problem. The fluid components are assumed to be immiscible and are separated by material interface. We track the location of the interface using the level set approach and replace the energy equation in the original model with the corresponding pressure equation in its neighborhoods. In these neighboring areas we solve the resulting nonconservative system using a path-conservative central-upwind scheme, while in the rest of the computational domain, a central-upwind scheme is used to numerically solve the original conservative system. We first develop a finite-volume method of the second order and then extend it to the fifth order via the finite-difference alternative WENO (A-WENO) framework. In order to reduce oscillations, we switch from A-WENO back to second-order central-upwind scheme in certain nonsmooth parts of the computational solution. We illustrate the performance of the new hybrid methods on a number of one- and two-dimensional examples including the shock–bubble interaction tests.

✉ Shaoshuai Chu
11930702@mail.sustech.edu.cn

Alina Chertock
chertock@math.ncsu.edu

Alexander Kurganov
alexander@sustech.edu.cn

[1] Department of Mathematics, North Carolina State University, Raleigh, NC 27695, USA

[2] Department of Mathematics, Southern University of Science and Technology, Shenzhen 518055, China

[3] Department of Mathematics, SUSTech International Center for Mathematics and Guangdong Provincial Key Laboratory of Computational Science and Material Design, Southern University of Science and Technology, Shenzhen 518055, China

# 1 Introduction

In this paper, we develop a new numerical method for multifluids, which are assumed to be immiscible and compressible. Assuming that all fluid components can be described by a single velocity and a single pressure, the governing equations in the two-dimensional (2-D) case read as:

$$\rho_t + (\rho u)_x + (\rho v)_y = 0, \tag{1.1}$$

$$(\rho u)_t + (\rho u^2 + p)_x + (\rho u v)_y = 0, \tag{1.2}$$

$$(\rho v)_t + (\rho u v)_x + (\rho v^2 + p)_y = 0, \tag{1.3}$$

$$E_t + [u(E + p)]_x + [v(E + p)]_y = 0. \tag{1.4}$$

Here, $x$ and $y$ are spatial variables, $t$ is time and $\rho(x, y, t), u(x, y, t), v(x, y, t)$ and $E(x, y, t)$ are the density, $x$- and $y$-velocities, and total energy, respectively. The system is completed through the following equations of state (EOS) for each of the fluid components:

$$p = (\gamma - 1)\Big[E - \frac{\rho}{2}(u^2 + v^2)\Big] - \gamma p_\infty, \tag{1.5}$$

where the parameters $\gamma$ and $p_\infty$ represent the specific heat ratios and the stiffness parameters, respectively, with $p_\infty = 0$ corresponding to the ideal gas case. In this paper, we consider a multifluid problem with two components and assume that $\gamma = \gamma_I$, $p_\infty = p_{\infty,I}$ and $\gamma = \gamma_{II}$, $p_\infty = p_{\infty,II}$ for the first and second fluid components, respectively.

For multifluid problems, the fluid components are usually identified by the variable $\phi$, which can be taken as a state variable, such as the specific heat ratio $\gamma$ (or any function of it), or the mass fraction of the fluid component in the fluid mixture, or a level-set function whose zero level-set defines the interface between the fluid components; see [1,2,12,29,34]. In all of the cases, $\phi$ propagates with the fluid velocity satisfying the equation

$$\phi_t + u\phi_x + v\phi_y = 0, \tag{1.6}$$

which may be combined with the first equation in (1.1) and recast in the conservation form:

$$(\rho\phi)_t + (\rho u\phi)_x + (\rho v\phi)_y = 0. \tag{1.7}$$

It should be noted that there are situations, like bubbly flows or liquid suspensions, in which the number of interfaces is too large to be tracked. In such cases, it is widely accepted that average flow characteristics are sufficient to describe the relevant macroscopic dynamics. Averaging the fluid equations yields multiphase models in which at every point in space, all fluid components co-exist with certain volume fractions. In the two fluid case, the corresponding 2-velocity 2-pressure compressible model was first proposed in [5] to describe the deflagration-to-detonation transition in porous granular explosives mixed with gaseous products of combustion and then extended to gas–gas and gas–liquid flow models in [34]. In the one-dimensional (1-D) case, the model from [34] is also refer to as the "seven-equation" model. It may be reduced to the so-called "six-equation" model, several "five-equation" models, and the "four-equation" model studied in this paper; see, e.g., [23,24] and the references therein.

The system (1.1)–(1.5), (1.7) is a system of hyperbolic conservation laws, whose solutions are expected to develop complicated nonlinear wave structures that may include shocks, rarefactions and contact discontinuities. Computing such solutions numerically requires the use of high-resolution shock-capturing numerical methods with finite-volume (FV) schemes

being a popular choice; see, e.g., the monographs [17,25,38] and references therein. It is well-known, however, that applying single fluid FV methods to the multifluid system (1.1)–(1.5), (1.7) may lead to significant pressure and velocity oscillations, which typically originate near the material interface and then spread all over the computational domain; see, e.g., [1,20]. This happens since in the cells where the interface is located the fluids are artificially mixed, with the mixed cell average values often being nonphysical. Therefore, one needs to design special multifluid algorithms.

A number of FV methods solving compressible multifluids problems were proposed. When the interface is tracked using a FV approach to solve either (1.6) or (1.7), one can only obtain the information about a set of cells, in which the interface is located. In this situation, one may need to consider cells occupied by different fluids—the so-called "mixed" cells. There were attempts to derive special equations of state for the "mixed" cells using either $\gamma$ or mass fraction values obtained from either (1.6) or (1.7); see, e.g., [3,36]. This technique, however, has several limitations and may lead to nonphysical jumps near the material fronts. A more accurate "mixed" cell information can be obtained by considering the so-called five-equation models [4,7], in which the continuity equation (1.1) is replaced with the corresponding equation for each fluid fraction. A simpler and fully conservative method was developed in [35], where the pressure and velocity kept constant across the material interface. This approach is very robust for tracking contact waves but may suffer obvious drawbacks when strong shocks pass through the fluid interface. An alternative way of treating multifluids was introduced in [2,12]. The material interface was placed not inside a cell but at a cell interface at which two sets of fluxes are computed using the extrapolation of the material data across the interface, which results in nonconservative ghost fluid methods, which are capable of accurately tracking the material interface.

A different interface tracking method, which is also capable of sharply resolving contact waves at material interfaces, was introduced in [9]; see also [41]. There, the unreliable "mixed" cell data have never been never used. Instead the reliable single fluid data from the both sides of the interface is used to interpolate the missing "mixed" cell information. The interpolation is carried out in the phase space by solving the corresponding Riemann problem; see [9] for details. It is worth pointing out that while the ghost fluid and interface tracking methods are very robust in the 1-D case, their extensions to multidimensional problems are rather cumbersome. For high-order WENO schemes for compressible multifluids, we refer the reader to [11,16,19,31,32].

In this paper, our primary objective is to develop a robust and highly accurate hybrid algorithm based on switching between the pressure and energy equations. Following the idea in [20], we use the level-set function (1.7) to identify the "mixed" cells, in which we replace the conservative energy equation with the nonconservative pressure one. We carefully derive the pressure equation, which in the multifluid case contains the nonconservative term responsible for the jumps in fluid parameters across the material interface. The obtained nonconservative system is then solved in the "mixed" cells using the path-conservative central upwind (PCCU) scheme introduced in [6]. In the rest of the computational domain, we solve the original conservative system (1.1)–(1.5), (1.7) using the central-upwind (CU) scheme from [8,21]. Our method is first designed in the 1-D case and then easily extended to the 2-D case with the PCCU method applied in a component-wise manner. We also extend the proposed hybrid algorithm to higher order using the framework of the fifth-order finite-difference alternative WENO (A-WENO) schemes developed in [18,27,28,39,40]. To this end, we use the A-WENO scheme with the CU fluxes to solve the original conservative system away from material interfaces and the path-conservative A-WENO schemes, recently proposed in [10], to solve the nonconservative system near the material interfaces.

The paper is organized as follows. In Sect. 2, we describe the proposed hybrid multifluid algorithms. We first present the 1-D algorithm in Sect. 2.1, and then extend it to the 2-D case in Sect. 2.2. In Sect. 3, we present both the 1-D (Sect. 3.1) and 2-D (Sect. 3.2) numerical results.

## 2 Hybrid Multifluid Algorithms

We now present the new hybrid multifluid algorithms based on the CU and PCCU schemes.

### 2.1 One-Dimensional Algorithm

We begin with the 1-D Euler equations of gas dynamics,

$$\rho_t + (\rho u)_x = 0, \tag{2.1}$$

$$(\rho u)_t + (\rho u^2 + p)_x = 0, \tag{2.2}$$

$$E_t + [u(E + p)]_x = 0, \tag{2.3}$$

combined with the EOS

$$p = (\gamma - 1)\Big[E - \frac{1}{2}\rho u^2\Big] - \gamma p_\infty, \tag{2.4}$$

and the equation

$$(\rho\phi)_t + (\rho u\phi)_x = 0, \tag{2.5}$$

where $\phi$ is the level-set function used to determine the position of the interface.

We consider the 1-D system (2.1)–(2.5) in a computational domain covered with the uniform cells $C_j := [x_{j-\frac{1}{2}}, x_{j+\frac{1}{2}}]$ of size $\Delta x$ centered at $x_j = (x_{j-\frac{1}{2}} + x_{j+\frac{1}{2}})/2$. We denote by $\overline{U}_j(t)$ the cell averages of $U(\cdot, t)$ over the corresponding intervals $C_j$:

$$\overline{U}_j(t) :\approx \frac{1}{\Delta x} \int_{C_j} U(x, t)\,\mathrm{d}x,$$

where $U := (\rho, \rho u, E, \rho\phi)^\top$ is a vector of conservative variables. Assuming that the cell average values $\{\overline{U}_j\}$ are available at a certain time $t \geq 0$, we compute the point values $\phi_j = (\overline{\rho\phi})_j / \overline{\rho}_j$ and the corresponding values of $\gamma$ and $p_\infty$ at the center of each cell:

$$\gamma_j = \begin{cases} \gamma_I, & \text{if } \phi_j > 0, \\ \gamma_{II}, & \text{otherwise,} \end{cases} \qquad (p_\infty)_j = \begin{cases} p_{\infty,I}, & \text{if } \phi_j > 0, \\ p_{\infty,II}, & \text{otherwise.} \end{cases} \tag{2.6}$$

For the simplicity of presentation, we assume that there is only one material interface present in the computational domain and we use the point values $\phi_j(t)$ to determine its location at each time level, that is, we set that the material interface is located in either $C_J$ or $C_{J+1}$, if $\phi_J(t) \cdot \phi_{J+1}(t) \leq 0$. Cells $C_J$ and $C_{J+1}$ are referred to as the interface cells, for which we follow the hybrid approach introduced in [20] and replace the energy equation (2.3) with the pressure one:

$$p_t + (up)_x = -\big[(\gamma - 1)p + \gamma p_\infty\big]u_x. \tag{2.7}$$

The case of a larger, but finite number of interfaces can be treated similarly.

Note that the pressure equation (2.7) is obtained by expressing the total energy $E$ in terms of $\rho$, $u$ and $p$ from the EOS (2.4), substituting it into the energy equation (2.3) and then using

the density and momentum equations (2.1) and (2.2) to eliminate the $\rho_t$ and $(\rho u)_t$ terms, respectively.

The proposed multifluid hybrid algorithms is based on implementing different numerical schemes in different parts of the computational domain. Specifically, we solve the conservative system (2.1)–(2.5) using the CU scheme outside of the interface regions, while inside such regions, we solve the nonconservative system (2.1), (2.2), (2.4), (2.5), (2.7) using the PCCU scheme. Notice that our hybrid approach is generically nonconservative, but the conservation error is expected to decay when $\Delta x$ decreases as we solve the pressure equation (2.7) in a small neighborhood of the material interface only.

In Sects. 2.1.1–2.1.4, we describe the semi-discrete second-order CU and PCCU schemes and their fifth-order extensions developed within the A-WENO framework.

### 2.1.1 Semi-Discrete Central-Upwind (CU) Scheme

We first provide a brief description of the 1-D second-order CU scheme. To this end, we rewrite the conservative system (2.1)–(2.5) in the vector form as

$$U_t + F(U)_x = 0, \tag{2.8}$$

where $F(U) = (\rho u, \rho u^2 + p, u(E + p), \rho u \phi)^\top$ and apply the CU scheme from [21] in each cell $C_j : j \notin \{J, J + 1\}$. The latter results in the following system of ODEs:

$$\frac{d\overline{U}_j}{dt} = -\frac{H_{j+\frac{1}{2}} - H_{j-\frac{1}{2}}}{\Delta x}, \quad j \notin \{J, J + 1\},$$

where

$$H_{j+\frac{1}{2}} = \frac{a^+_{j+\frac{1}{2}} F(U^-_{j+\frac{1}{2}}) - a^-_{j+\frac{1}{2}} F(U^+_{j+\frac{1}{2}})}{a^+_{j+\frac{1}{2}} - a^-_{j+\frac{1}{2}}} + \frac{a^+_{j+\frac{1}{2}} a^-_{j+\frac{1}{2}}}{a^+_{j+\frac{1}{2}} - a^-_{j+\frac{1}{2}}} \left( U^+_{j+\frac{1}{2}} - U^-_{j+\frac{1}{2}} - Q_{j+\frac{1}{2}} \right). \tag{2.9}$$

Notice that all of the indexed quantities depend on $t$, but from now on we will omit this dependence for the sake of brevity.

In (2.9), $U^\pm_{j+\frac{1}{2}}$ are the right/left-sided values of $U$ constructed in the following way. From the available cell averages $\overline{U}_j = \left( \overline{\rho}_j, (\overline{\rho u})_j, \overline{E}_j, (\overline{\rho \phi})_j \right)^\top$, we first compute cell centered values of the velocity $u$ and pressure $p$,

$$u_j = \frac{(\overline{\rho u})_j}{\overline{\rho}_j}, \quad p_j = (\gamma_j - 1) \left[ \overline{E}_j - \frac{\left( (\overline{\rho u})_j \right)^2}{2\overline{\rho}_j} \right] - \gamma_j (p_\infty)_j,$$

and apply a piecewise linear reconstruction to the primitive variables $V = (\rho, u, p, \phi)^\top$:

$$\widetilde{V}_j(x) = V_j + (V_x)_j(x - x_j), \quad x \in C_j, \tag{2.10}$$

and a piecewise constant approximation to $\gamma$ and $p_\infty$:

$$\widetilde{\gamma}_j(x) \equiv \gamma_j \quad \text{and} \quad (\widetilde{p}_\infty)_j(x) \equiv (p_\infty)_j, \quad x \in C_j, \tag{2.11}$$

where both $\gamma_j$ and $(p_\infty)_j$ are defined in (2.6). Since here we restrict our consideration to the case of a single material interface, we have

$$\widetilde{\gamma}_j(x) = \begin{cases} \gamma_I, & \text{if } x < x_{J+\frac{1}{2}}, \\ \gamma_{II}, & \text{otherwise,} \end{cases} \qquad (\widetilde{p}_\infty)_j(x) = \begin{cases} p_{\infty,I}, & \text{if } x < x_{J+\frac{1}{2}}, \\ p_{\infty,II}, & \text{otherwise.} \end{cases} \tag{2.12}$$

In order to ensure a non-oscillatory nature of the piecewise linear reconstruction (2.10), one needs to to compute the slopes $(\boldsymbol{V}_x)_j$ with the help of a nonlinear limiter. In the numerical experiments reported in Sect. 3, we have used a generalized minmod limiter [26,30,37]:

$$
(\boldsymbol{V}_x)_j = \mathrm{minmod}\left( \theta\, \frac{\overline{\boldsymbol{V}}_j - \overline{\boldsymbol{V}}_{j-1}}{\Delta x},\, \frac{\overline{\boldsymbol{V}}_{j+1} - \overline{\boldsymbol{V}}_{j-1}}{2\Delta x},\, \theta\, \frac{\overline{\boldsymbol{V}}_{j+1} - \overline{\boldsymbol{V}}_j}{\Delta x} \right),
$$

applied to the vector quantity $\boldsymbol{V}$ in a component-wise manner. Here, the minmod function is defined as

$$
\mathrm{minmod}(z_1, z_2, \cdots) := \begin{cases} \min_{j}\{z_j\}, & \text{if } z_j > 0\ \forall j, \\[4pt] \max_{j}\{z_j\}, & \text{if } z_j < 0\ \forall j, \\[4pt] 0, & \text{otherwise.} \end{cases} \tag{2.13}
$$

The parameter $\theta$ can be used to control the amount of numerical dissipation present in the resulting scheme and larger $\theta$'s correspond to less dissipative but, in general, more oscillatory reconstructions.

We then use (2.10) and (2.12) to obtain

$$
\boldsymbol{V}^+_{j+\frac{1}{2}} := \widetilde{\boldsymbol{V}}_j(x_{j+\frac{1}{2}} + 0) = \boldsymbol{V}_{j+1} - \frac{\Delta x}{2}(\boldsymbol{V}_x)_{j+1},
$$
$$
\boldsymbol{V}^-_{j+\frac{1}{2}} := \widetilde{\boldsymbol{V}}_j(x_{j-\frac{1}{2}} - 0) = \boldsymbol{V}_j + \frac{\Delta x}{2}(\boldsymbol{V}_x)_{j+1}, \tag{2.14}
$$
$$
\gamma^{\pm}_{j+\frac{1}{2}} = \gamma_j = \gamma_{j+1}, \quad (p_\infty)^{\pm}_{j+\frac{1}{2}} = (p_\infty)_j = (p_\infty)_{j+1}, \tag{2.15}
$$

and the corresponding point values

$$
\boldsymbol{U}^{\pm}_{j+\frac{1}{2}} = \left( \rho^{\pm}_{j+\frac{1}{2}},\, \rho^{\pm}_{j+\frac{1}{2}} u^{\pm}_{j+\frac{1}{2}},\, \frac{p^{\pm}_{j+\frac{1}{2}} + \gamma^{\pm}_{j+\frac{1}{2}} (p_\infty)^{\pm}_{j+\frac{1}{2}}}{\gamma^{\pm}_{j+\frac{1}{2}} - 1} + \frac{\rho^{\pm}_{j+\frac{1}{2}} (u^{\pm}_{j+\frac{1}{2}})^2}{2},\, \rho^{\pm}_{j+\frac{1}{2}} \phi^{\pm}_{j+\frac{1}{2}} \right)^{\top}.
$$

Note that (2.15) is true since we now consider single-fluid parts of the computational domain only, that is, $j \notin \{J, J+1\}$.

**Remark 2.1** We use the piecewise linear reconstruction of the primitive variables $\boldsymbol{V}$ since both the pressure and velocity are continuous across the material interface.

The term $\boldsymbol{Q}_{j+\frac{1}{2}}$ in (2.9) represents a built-in "anti-diffusion" and it is given by (see [21]):

$$
\boldsymbol{Q}_{j+\frac{1}{2}} = \mathrm{minmod}\left( \boldsymbol{U}^+_{j+\frac{1}{2}} - \boldsymbol{U}^*_{j+\frac{1}{2}},\, \boldsymbol{U}^*_{j+\frac{1}{2}} - \boldsymbol{U}^-_{j+\frac{1}{2}} \right), \tag{2.16}
$$

where

$$
\boldsymbol{U}^*_{j+\frac{1}{2}} = \frac{a^+_{j+\frac{1}{2}} \boldsymbol{U}^+_{j+\frac{1}{2}} - a^-_{j+\frac{1}{2}} \boldsymbol{U}^-_{j+\frac{1}{2}} - \left\{ \boldsymbol{F}(\boldsymbol{U}^+_{j+\frac{1}{2}}) - \boldsymbol{F}(\boldsymbol{U}^-_{j+\frac{1}{2}}) \right\}}{a^+_{j+\frac{1}{2}} - a^-_{j+\frac{1}{2}}}. \tag{2.17}
$$

Finally, $a^{\pm}_{j+\frac{1}{2}}$ are the one-sided local speeds of propagation obtained from the largest and the smallest eigenvalues of the Jacobian $\frac{\partial \boldsymbol{F}}{\partial \boldsymbol{U}}$ as follows:

$$a^+_{j+\frac{1}{2}} = \left\{ u^-_{j+\frac{1}{2}} + c^-_{j+\frac{1}{2}}, u^+_{j+\frac{1}{2}} + c^+_{j+\frac{1}{2}}, 0 \right\}, \quad a^-_{j+\frac{1}{2}} = \left\{ u^-_{j+\frac{1}{2}} - c^-_{j+\frac{1}{2}}, u^+_{j+\frac{1}{2}} - c^+_{j+\frac{1}{2}}, 0 \right\},$$

(2.18)

where $c := \sqrt{\gamma(p + p_\infty)/\rho}$.

### 2.1.2 Path-Conservative Central-Upwind (PCCU) Scheme

In order to design a second-order PCCU scheme for the system (2.1), (2.2), (2.4), (2.5) and (2.7), we first rewrite it in the following vector form:

$$\mathcal{U}_t + F(\mathcal{U})_x = B(\mathcal{U})\mathcal{U}_x,$$

(2.19)

where $\mathcal{U} = (\rho, \rho u, p, \rho\phi)^\top$, $\mathcal{F}(\mathcal{U}) = (\rho u, \rho u^2 + p, pu, \rho u\phi)^\top$, and

$$B(\mathcal{U}) = \begin{pmatrix} 0 & 0 & 0 & 0 \\ 0 & 0 & 0 & 0 \\ \dfrac{[(\gamma-1)p + \gamma p_\infty]u}{\rho} & \dfrac{(1-\gamma)p - \gamma p_\infty}{\rho} & 0 & 0 \\ 0 & 0 & 0 & 0 \end{pmatrix}.$$

(2.20)

Applying the PCCU scheme from [6] to the system (2.19), (2.20), we arrive at the following semi-discretization for $\mathcal{U}_j = \left( \overline{\rho}_j, \overline{(\rho u)}_j, p_j, \overline{(\rho\phi)}_j \right)^\top$:

$$\frac{\mathrm{d}\mathcal{U}_j}{\mathrm{d}t} = -\frac{1}{\Delta x}\left[ \mathcal{H}_{j+\frac{1}{2}} - \mathcal{H}_{j-\frac{1}{2}} - B_j - \frac{a^+_{j-\frac{1}{2}}}{a^+_{j-\frac{1}{2}} - a^-_{j-\frac{1}{2}}} B_{\Psi, j-\frac{1}{2}} + \frac{a^-_{j+\frac{1}{2}}}{a^+_{j+\frac{1}{2}} - a^-_{j+\frac{1}{2}}} B_{\Psi, j+\frac{1}{2}} \right],$$

$$j \notin \{J, J+1\},$$

where

$$\mathcal{H}_{j+\frac{1}{2}} = \frac{a^+_{j+\frac{1}{2}}\mathcal{F}(\mathcal{U}^-_{j+\frac{1}{2}}) - a^-_{j+\frac{1}{2}}\mathcal{F}(\mathcal{U}^+_{j+\frac{1}{2}})}{a^+_{j+\frac{1}{2}} - a^-_{j+\frac{1}{2}}} + \frac{a^+_{j+\frac{1}{2}}a^-_{j+\frac{1}{2}}}{a^+_{j+\frac{1}{2}} - a^-_{j+\frac{1}{2}}}\left( \mathcal{U}^+_{j+\frac{1}{2}} - \mathcal{U}^-_{j+\frac{1}{2}} - Q_{j+\frac{1}{2}} \right),$$

$$B_j = \left( 0, 0, -\int_{C_j} \left[ (\widetilde{\gamma}_j(x) - 1)\widetilde{p}_j(x) + \widetilde{\gamma}_j(x)(\widetilde{p}_\infty)_j(x) \right] (u_x)_j \, \mathrm{d}x, 0 \right)^\top,$$

(2.21)

$$B_{\Psi, j+\frac{1}{2}} = \left( 0, 0, \int_0^1 B(p_{j+\frac{1}{2}}(s))\frac{\mathrm{d}u_{j+\frac{1}{2}}}{\mathrm{d}s}\,\mathrm{d}s, 0 \right)^\top.$$

(2.22)

In order to evaluate the integral in (2.21), we use the piecewise linear reconstructions of $p$ and $u$ from (2.14) to obtain

$$B^{(3)}_j = -\frac{1}{2}\Big[ (\gamma^-_{j+\frac{1}{2}} - 1)p^-_{j+\frac{1}{2}} + (\gamma^+_{j-\frac{1}{2}} - 1)p^+_{j-\frac{1}{2}}$$

$$+ \gamma^-_{j+\frac{1}{2}}(p_\infty)^-_{j+\frac{1}{2}} + \gamma^+_{j-\frac{1}{2}}(p_\infty)^+_{j-\frac{1}{2}} \Big](u^-_{j+\frac{1}{2}} - u^+_{j-\frac{1}{2}}), \quad j \in \{J, J+1\}.$$

(2.23)

For the integral in (2.22), one needs to select a path connecting the points $(u^-_{j+\frac{1}{2}}, p^-_{j+\frac{1}{2}})$ and $(u^+_{j+\frac{1}{2}}, p^+_{j+\frac{1}{2}})$. In this paper, we use a linear path, that is,

$$p_{j+\frac{1}{2}}(s) = p^+_{j+\frac{1}{2}} + (1-s)p^-_{j+\frac{1}{2}}, \quad u_{j+\frac{1}{2}}(s) = u^+_{j+\frac{1}{2}} + (1-s)u^-_{j+\frac{1}{2}},$$

which results in

$$
\begin{aligned}
B^{(3)}_{\Psi, j+\frac{1}{2}} = -\frac{1}{2}\Big[ & (\gamma^+_{j+\frac{1}{2}} - 1)p^+_{j+\frac{1}{2}} + (\gamma^-_{j+\frac{1}{2}} - 1)p^-_{j+\frac{1}{2}} \\
& + \gamma^+_{j+\frac{1}{2}}(p_\infty)^+_{j+\frac{1}{2}} + \gamma^-_{j+\frac{1}{2}}(p_\infty)^-_{j+\frac{1}{2}} \Big](u^+_{j+\frac{1}{2}} - u^-_{j+\frac{1}{2}}), \quad j \in \{J-1, J, J+1\}.
\end{aligned}
$$

Note that according to (2.11), both $\gamma$ and $p_\infty$ have jumps at the material interface $x = x_{J+\frac{1}{2}}$ so that

$$
\begin{cases}
\gamma^\pm_{J-\frac{1}{2}} = \gamma^-_{J+\frac{1}{2}} = \gamma_J, \\
\gamma^\pm_{J+\frac{3}{2}} = \gamma^+_{J+\frac{1}{2}} = \gamma_{J+1}
\end{cases}
\quad \text{and} \quad
\begin{cases}
(p_\infty)^\pm_{J-\frac{1}{2}} = (p_\infty)^-_{J+\frac{1}{2}} = (p_\infty)_J, \\
(p_\infty)^\pm_{J+\frac{3}{2}} = (p_\infty)^+_{J+\frac{1}{2}} = (p_\infty)_{J+1}.
\end{cases}
\tag{2.24}
$$

As in Sect. 2.1.1, we then reconstruct the primitive variables $\boldsymbol{V}$ to obtain the point values $\boldsymbol{\mathcal{U}}^\pm_{j+\frac{1}{2}}$. The built-in "anti-diffusion" term $\boldsymbol{Q}_{j+\frac{1}{2}}$ is given by (2.16), (2.17) but with $\boldsymbol{U}$ and $\boldsymbol{F}$ replaced with $\boldsymbol{\mathcal{U}}$ and $\boldsymbol{\mathcal{F}}$, respectively. The local speeds $a^\pm_{j+\frac{1}{2}}$ are still computed using (2.18) with $\gamma^\pm_{j+\frac{1}{2}}$ and $(p_\infty)^\pm_{j+\frac{1}{2}}$ given by (2.24).

**Remark 2.2** Notice that the "anti-diffusion" term $\boldsymbol{Q}_{j+\frac{1}{2}}$ was not present in the PCCU schemes in [6] as they were based on the earlier version of the central-upwind schemes introduced in [22]. On the contrary, the PCCU scheme presented in this section is based on a more recent version of the central-upwind schemes from [21].

### 2.1.3 Fifth-Order A-WENO Scheme

In order to increase the resolution of contact waves and smooth parts of the solution, one may want to use a higher-order extension of the FV scheme presented above. In this section, we show how to design such an extension using an A-WENO finite-difference approach. According to this approach, the point values of the solution of (2.8) are evolved in time by solving the following system of ODEs:

$$
\frac{d\boldsymbol{U}_j}{dt} = -\frac{\mathfrak{H}_{j+\frac{1}{2}} - \mathfrak{H}_{j-\frac{1}{2}}}{\Delta x}.
$$

Here, $\mathfrak{H}_{j+\frac{1}{2}}$ is the fifth-order numerical flux defined by

$$
\mathfrak{H}_{j+\frac{1}{2}} = \boldsymbol{H}_{j+\frac{1}{2}} - \frac{1}{24}(\Delta x)^2(\boldsymbol{F}_{xx})_{j+\frac{1}{2}} + \frac{7}{5760}(\Delta x)^4(\boldsymbol{F}_{xxxx})_{j+\frac{1}{2}};
\tag{2.25}
$$

see [18,27,28,39,40] for its derivation. In (2.25), $\boldsymbol{H}_{j+\frac{1}{2}}$ is the FV numerical flux (we use the CU flux (2.9)), and the higher-order convection terms $(\boldsymbol{F}_{xx})_{j+\frac{1}{2}}$ and $(\boldsymbol{F}_{xxxx})_{j+\frac{1}{2}}$ are computed using the second- and fourth-order finite-differences as follows:

$$
\begin{aligned}
(\boldsymbol{F}_{xx})_{j+\frac{1}{2}} &= \frac{1}{48(\Delta x)^2}(-5\boldsymbol{F}_{j-2} + 39\boldsymbol{F}_{j-1} - 34\boldsymbol{F}_j - 34\boldsymbol{F}_{j+1} + 39\boldsymbol{F}_{j+2} - 5\boldsymbol{F}_{j+3}), \\
(\boldsymbol{F}_{xxxx})_{j+\frac{1}{2}} &= \frac{1}{2(\Delta x)^4}(\boldsymbol{F}_{j-2} - 3\boldsymbol{F}_{j-1} + 2\boldsymbol{F}_j + 2\boldsymbol{F}_{j+1} - 3\boldsymbol{F}_{j+2} + \boldsymbol{F}_{j+3}).
\end{aligned}
\tag{2.26}
$$

It should be emphasized that the resulting scheme will be fifth-order accurate provided the one-sided point values $\boldsymbol{U}^\pm_{j+\frac{1}{2}}$ used in the numerical flux $\boldsymbol{H}_{j+\frac{1}{2}}$ are also fifth-order accurate. In this paper, we use the fifth-order alternative WENO polynomial interpolation procedure

with the Z-type weights (WENO-Z) (see [18,27,40]) applied once again to the primitive variables $V_j$ in a component-wise manner. For the sake of brevity, we only introduce how to compute $V^-_{j+\frac{1}{2}}$, while $V^+_{j+\frac{1}{2}}$ can be obtained using the mirror-symmetric stencil.

Equipped with the point values $V_j$, we first compute three parabolic interpolants $\mathcal{P}_k(x) = (\mathcal{P}_1(x), \mathcal{P}_2(x), \mathcal{P}_3(x))^\top$ using the point values $\left\{(x_{j-2+k}, V_{j-2+k}), (x_{j-1+k}, V_{j-1+k}),\right.$ $\left.(x_{j+k}, V_{j+k})\right\}$ for $k = 0, 1, 2$. The fifth-order WENO-Z interpolations for the $i$th component of $V$ ($i = 1, 2, 3, 4$) are then given by

$$(V^{(i)}_{j+\frac{1}{2}})^- = \sum_{k=0}^{2} \omega_k^{(i)} \mathcal{P}_k^{(i)}(x_{j+\frac{1}{2}}), \tag{2.27}$$

where

$$\mathcal{P}_0^{(i)}(x_{j+\frac{1}{2}}) = \frac{3}{8}V^{(i)}_{j-2} - \frac{5}{4}V^{(i)}_{j-1} + \frac{15}{8}V^{(i)}_j,$$

$$\mathcal{P}_1^{(i)}(x_{j+\frac{1}{2}}) = -\frac{1}{8}V^{(i)}_{j-1} + \frac{3}{4}V^{(i)}_j + \frac{3}{8}V^{(i)}_{j+1},$$

$$\mathcal{P}_2^{(i)}(x_{j+\frac{1}{2}}) = \frac{3}{8}V^{(i)}_j + \frac{3}{4}V^{(i)}_{j+1} - \frac{1}{8}V^{(i)}_{j+2}.$$

The weights $\omega_k^{(i)}$ in (2.27) are computed by

$$\omega_k^{(i)} = \frac{\alpha_k^{(i)}}{\alpha_0^{(i)} + \alpha_1^{(i)} + \alpha_2^{(i)}}, \quad \alpha_k^{(i)} = d_k\left[1 + \left(\frac{\tau_5^{(i)}}{\beta_k^{(i)} + \varepsilon}\right)^p\right]$$

with $d_0 = \frac{1}{16}, d_1 = \frac{5}{8}, d_2 = \frac{5}{16}, \beta_k^{(i)}$ defined by

$$\beta_k^{(i)} = \sum_{\ell=1}^{2}(\Delta x)^{2\ell-1}\int_{C_j}\left(\frac{\partial^\ell \mathcal{P}_k^{(i)}}{\partial x^\ell}\right)^2 dx, \quad k = 0, 1, 2,$$

and $\tau_5^{(i)} = |\beta_2^{(i)} - \beta_0^{(i)}|$. In all of the numerical examples reported in Sect. 3, we have chosen $p = 2$ and $\varepsilon = 10^{-12}$.

### 2.1.4 Path-Conservative A-WENO Scheme

In order to increase the accuracy inside the interface region $\{C_J, C_{J+1}\}$, one may use the path-conservative A-WENO scheme there. According to [10], this scheme reads as

$$\frac{d\mathcal{U}_j}{dt} = -\frac{1}{\Delta x}\left[\mathcal{H}_{j+\frac{1}{2}} - \mathcal{H}_{j-\frac{1}{2}} - B_j - \frac{a^+_{j-\frac{1}{2}}}{a^+_{j-\frac{1}{2}} - a^-_{j-\frac{1}{2}}}B_{\Psi,j-\frac{1}{2}} + \frac{a^-_{j+\frac{1}{2}}}{a^+_{j+\frac{1}{2}} - a^-_{j+\frac{1}{2}}}B_{\Psi,j+\frac{1}{2}}\right]$$

$$+ \frac{\Delta x}{24}\left[(K_{xx})_{j+\frac{1}{2}} - (K_{xx})_{j-\frac{1}{2}}\right] - \frac{7}{5760}(\Delta x)^3\left[(K_{xxxx})_{j+\frac{1}{2}} - (K_{xxxx})_{j-\frac{1}{2}}\right],$$

where $\mathcal{H}_{j+\frac{1}{2}}, B_j, B_{\Psi,j+\frac{1}{2}}$ and $a^\pm_{j+\frac{1}{2}}$ are defined as in Sect. 2.1.2, $\mathcal{U}^\pm_{j+\frac{1}{2}}$ are computed using the fifth-order WENO-Z interpolant described in Sect. 2.1.3, and $(K_{xx})_{j+\frac{1}{2}}$ and $(K_{xxxx})_{j+\frac{1}{2}}$

are finite-difference approximations of the second- and fourth-order spatial derivatives of the function

$$K(\mathcal{U}(\cdot, t)) = \mathcal{F}(\mathcal{U}(x, t)) - \int_{-\infty}^{x} B(\mathcal{U}(\xi, t))\mathcal{U}_x(\xi, t)\, d\xi.$$

The derivatives of $K$ are given by (see [10])

$$(K_{xx})_{j+\frac{1}{2}} = (\mathcal{F}_{xx})_{j+\frac{1}{2}} - [(B(\mathcal{U})\mathcal{U}_x)_x]_{j+\frac{1}{2}}$$
$$(K_{xxxx})_{j+\frac{1}{2}} = (\mathcal{F}_{xxxx})_{j+\frac{1}{2}} - [(B(\mathcal{U})\mathcal{U}_x)_{xxx}]_{j+\frac{1}{2}},$$

where $(\mathcal{F}_{xx})_{j+\frac{1}{2}}$ and $(\mathcal{F}_{xxxx})_{j+\frac{1}{2}}$ are computed in the same way as $(F_{xx})_{j+\frac{1}{2}}$ and $(F_{xxxx})_{j+\frac{1}{2}}$ were computed in (2.26), but with $F$ replaced by $\mathcal{F}$, and

$$[(B(\mathcal{U})\mathcal{U}_x)_x]_{j+\frac{1}{2}} = \frac{1}{24\Delta x}\Big\{ -(B(\mathcal{U})\mathcal{U}_x)_{j+2} + 27(B(\mathcal{U})\mathcal{U}_x)_{j+1} - 27(B(\mathcal{U})\mathcal{U}_x)_j$$
$$+(B(\mathcal{U})\mathcal{U}_x)_{j-1} \Big\},$$

$$[(B(\mathcal{U})\mathcal{U}_x)_{xxx}]_{j+\frac{1}{2}} = \frac{1}{(\Delta x)^3}\Big\{ (B(\mathcal{U})\mathcal{U}_x)_{j+2} - 3(B(\mathcal{U})\mathcal{U}_x)_{j+1} + 3(B(\mathcal{U})\mathcal{U}_x)_j$$
$$-(B(\mathcal{U})\mathcal{U}_x)_{j-1} \Big\}.$$

Here, $(B(\mathcal{U})\mathcal{U}_x)_m = B(\mathcal{U}_m)(\mathcal{U}_x)_m$, for $m = j-1, j, j+1, j+2$, and

$$(\mathcal{U}_x)_{j-1} = \frac{1}{12\Delta x}\Big(\mathcal{U}_{j+2} - 6\mathcal{U}_{j+1} + 18\mathcal{U}_j - 10\mathcal{U}_{j-1} - 3\mathcal{U}_{j-2}\Big),$$
$$(\mathcal{U}_x)_j = \frac{1}{12\Delta x}\Big(-\mathcal{U}_{j+2} + 8\mathcal{U}_{j+1} - 8\mathcal{U}_{j-1} + \mathcal{U}_{j-2}\Big),$$
$$(\mathcal{U}_x)_{j+1} = \frac{1}{12\Delta x}\Big(-\mathcal{U}_{j+3} + 8\mathcal{U}_{j+2} - 8\mathcal{U}_j + \mathcal{U}_{j-1}\Big),$$
$$(\mathcal{U}_x)_{j+2} = \frac{1}{12\Delta x}\Big(3\mathcal{U}_{j+3} + 10\mathcal{U}_{j+2} - 18\mathcal{U}_{j+1} + 6\mathcal{U}_j - \mathcal{U}_{j-1}\Big).$$

**Remark 2.3** In order to ensure the designed path-conservative A-WENO scheme is fifth-order accurate, the term $B_j$ needs to be evaluated using a fifth-order quadrature instead of the second-order one (2.23). In this paper, we use the Newton–Cotes approach presented in [10, §4].

### 2.1.5 Mixed-Order Approach

Even though the component-wise WENO interpolation is essentially non-oscillatory, the resulting A-WENO hybrid algorithm may still generate spurious oscillations. Using the local characteristic decomposition and performing the interpolation in terms of the primitive variables may help to reduce the magnitude of these oscillations but our numerical experiments clearly demonstrate that this would not lead to a robust multifluid algorithm.

We therefore propose the following mixed-order strategy. We first reconstruct all of the required the point values using the WENO-Z interpolant and then check whether the obtained point values satisfy monotonicity and smoothness conditions. The monotonicity is

checked for the following sequences: $\left(\rho_j, \rho^-_{j+\frac{1}{2}}, \rho^+_{j+\frac{1}{2}}, \rho_{j+1}\right)$, $\left(u_j, u^-_{j+\frac{1}{2}}, u^+_{j+\frac{1}{2}}, u_{j+1}\right)$ and $\left(p_j, p^-_{j+\frac{1}{2}}, p^+_{j+\frac{1}{2}}, p_{j+1}\right)$ and the smoothness is checked for the pressure. Namely, we say that the pressure profile is locally smooth if

$$\frac{|p^+_{j+\frac{1}{2}} - p^-_{j+\frac{1}{2}}|}{\max\left\{p^+_{j+\frac{1}{2}}, p^-_{j+\frac{1}{2}}\right\}} < \mathtt{C}(\Delta x)^2,$$

where $\mathtt{C}$ is a constant, which may be adjusted experimentally (in all of the 1-D numerical examples reported in Sect. 3, we have taken $\mathtt{C} = 1$).

If the above monotonicity or smoothness conditions are satisfied at $x = x_{j+\frac{1}{2}}$, we use the fifth-order A-WENO fluxes from Sects. 2.1.3 and 2.1.4. Otherwise, we locally switch to the second-order CU fluxes from Sects. 2.1.1 and 2.1.2, respectively.

## 2.2 Two-Dimensional Algorithm

We now consider the 2-D system (1.1)–(1.5), (1.7) and extend our 1-D hybrid algorithms to the 2-D case. The extension is rather straightforward as it is carried out in a dimension-by-dimension manner. We therefore only provide a brief description of the 2-D algorithm here.

We introduce a uniform Cartesian mesh with $x_j := j\Delta x$ and $y_k := k\Delta y$, and assume that the cell averages,

$$\overline{U}_{j,k} :\approx \frac{1}{\Delta x \Delta y} \iint_{C_{j,k}} U(x, y, t)\, \mathrm{d}y\, \mathrm{d}x,$$

have been computed at a certain time $t \geq 0$. Here, $C_{j,k} := [x_{j-\frac{1}{2}}, x_{j+\frac{1}{2}}] \times [y_{k-\frac{1}{2}}, y_{k+\frac{1}{2}}]$ are the FV cells and $U := (\rho, \rho u, \rho v, E, \rho\phi)^\top$.

As in the 1-D case, we first locate the position of the interface using the level-set function $\phi$, whose discrete values are computed by $\phi_{j,k} = (\overline{\rho\phi})_{j,k}/\overline{\rho}_{j,k}$. These values are in turn used to identify the so-called interface region. Specifically, we say that $C_{j,k}$ is an interface cell if either $\phi_{j,k} \cdot \phi_{j+1,k} < 0$, $\phi_{j,k} \cdot \phi_{j-1,k} < 0$, $\phi_{j,k} \cdot \phi_{j,k+1} < 0$ or $\phi_{j,k} \cdot \phi_{j,k-1} < 0$. We then replace the energy equation (1.4) with the pressure one,

$$p_t + (up)_x + (vp)_y = -\left[(\gamma - 1)p + \gamma p_\infty\right]u_x - \left[(\gamma - 1)p + \gamma v_y p_\infty\right]v_y, \quad (2.28)$$

in the interface region, where we will solve the system (1.1)–(1.3), (1.5), (1.7) and (2.28) instead of (1.1)–(1.5), (1.7).

We thus take the same hybrid approach as in the 1-D case. Away from the interface, we solve the conservative system (1.1)–(1.5), (1.7) using the 2-D semi-discrete CU scheme. Its second-order version is briefly described in Appendix A. A higher- (fifth-) order extension can be obtained within the finite-difference A-WENO approach by implementing the 1-D A-WENO numerical fluxes described in Sect. 2.1.2 in the $x$- and $y$-directions.

Inside the interface region, we solve the nonconservative pressure-based system (1.1)–(1.3), (1.5), (1.7) and (2.28) using either the second-order PCCU scheme or its fifth-order A-WENO extension recently proposed in [10]. In order to reduce the magnitude of the oscillations that might be present in the fifth-order results, we implement the same mixed-order strategy as the one presented in Sect. 2.1.5. We check the monotonicity at the middle of each cell interface. In the $x$-direction, we check whether the following sequences are

monotone:

$$\left(\overline{\rho}_{j,k}, \rho^{E}_{j,k}, \rho^{W}_{j+1,k}, \overline{\rho}_{j+1,k}\right), \left(u_{j,k}, u^{E}_{j,k}, u^{W}_{j+1,k}, u_{j+1,k}\right), \left(v_{j,k}, v^{E}_{j,k}, v^{W}_{j+1,k}, v_{j+1,k}\right),$$
$$\left(p_{j,k}, p^{E}_{j,k}, p^{W}_{j+1,k}, p_{j+1,k}\right).$$

Here, $u_{j,k}$, $v_{j,k}$ and $p_{j,k}$ are the point values of $u$, $v$ and $p$ at the cell centers given by (A.2), and $\rho^{E}_{j,k}, \rho^{W}_{j+1,k}, u^{E}_{j,k}, u^{W}_{j+1,k}, v^{E}_{j,k}, v^{W}_{j+1,k}, p^{E}_{j,k}$ and $p^{W}_{j+1,k}$ are the one-sided point values of $\rho$, $u$, $v$ and $p$ at the center of the cell interface given by (A.3). We also verify the local smoothness of the pressure there by checking whether the inequality

$$\frac{|p^{W}_{j+1,k} - p^{E}_{j,k}|}{\max\left\{p^{W}_{j+1,k}, p^{E}_{j,k}\right\}} < C(\Delta x)^2$$

is satisfied. Similarly, in the $y$-direction, the monotonicity is checked for the following sequences:

$$\left(\overline{\rho}_{j,k}, \rho^{N}_{j,k}, \rho^{S}_{j,k+1}, \overline{\rho}_{j,k+1}\right), \left(u_{j,k}, u^{N}_{j,k}, u^{S}_{j,k+1}, u_{j,k+1}\right), \left(v_{j,k}, v^{N}_{j,k}, v^{S}_{j,k+1}, v_{j,k+1}\right),$$
$$\left(p_{j,k}, p^{N}_{j,k}, p^{S}_{j,k+1}, p_{j,k+1}\right),$$

and the corresponding smoothness condition is

$$\frac{|p^{S}_{j,k+1} - p^{N}_{j,k}|}{\max\left\{p^{S}_{j,k+1}, p^{N}_{j,k}\right\}} < C(\Delta y)^2.$$

The one-sided point values $\rho^{N}_{j,k}, \rho^{S}_{j,k+1}, u^{N}_{j,k}, u^{S}_{j,k+1}, v^{N}_{j,k}, v^{S}_{j,k+1}, p^{N}_{j,k}$ and $p^{S}_{j,k+1}$ used in the above two formulae are defined in (A.3).

At the cell interfaces, where the above conditions fail, we replace the fifth-order A-WENO fluxes with the second-order CU fluxes.

**Remark 2.4** In all of the 2-D numerical examples reported in §3, we have taken $C = 5$.

## 3 Numerical Examples

In this section, five numerical experiments are conducted to test the proposed hybrid algorithm. In the first three 1-D examples, we test the shock-tube problem, the stiff shock-tube problem and the water–air model problem. In the last two 2-D examples, we present the results for the Helium and R22 bubble problems.

In all of the five examples, the time evolution is carried out using the three-stage third-order strong stability preserving (SSP) Runge–Kutta method [13,14] with the CFL number 0.3. The level-set function $\phi$ is initialized using

$$\phi(x, 0) = \begin{cases} 1, & x \in \Omega_I, \\ -1, & x \in \Omega_{II}, \end{cases} \quad \text{or} \quad \phi(x, y, 0) = \begin{cases} 1, & (x, y) \in \Omega_I, \\ -1, & (x, y) \in \Omega_{II}, \end{cases} \quad (3.1)$$

for the 1-D and 2-D examples, respectively. In (3.1), $\Omega_I$ and $\Omega_{II}$ are the parts of the computational domain initially filled by fluids I and II, respectively.
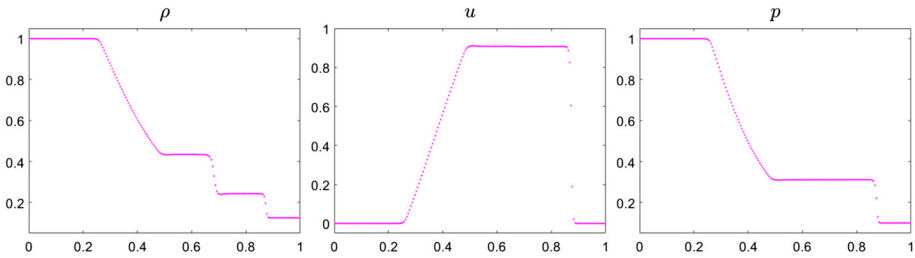
**Fig. 1** Example 1: Density ($\rho$), velocity ($u$) and pressure ($p$) computed by the mixed-order A-WENO scheme

### 3.1 One-Dimension Examples

We begin with the 1-D numerical examples. Our numerical experiments (not shown here for the sake of brevity) clearly indicate that in these three examples the second-order CU scheme and the mixed-order A-WENO scheme perform very similarly. We believe that this is related to the fact that the solutions of the studied Riemann problems do not contain complicated wave interaction and/or oscillatory parts of smooth solution. We will therefore show the results obtained by the mixed-order A-WENO scheme only.

In all of the 1-D examples, we measure the relative conservation error in the computation of the total energy $E$ using the following formula:

$$\text{err} := \frac{\sum_j \overline{E}_j(t) - \sum_j \overline{E}_j(0)}{\sum_j \overline{E}_j(0)}. \tag{3.2}$$

### Example 1—Shock-Tube Problem

In the first example, we consider the system (2.1)–(2.5) subject to the following initial conditions:

$$(\rho, u, p; \gamma, p_\infty) = \begin{cases} (1.000, 0, 1.0; 1.4, 0), & x < 0.5, \\ (0.125, 0, 0.1; 1.6, 0), & x > 0.5. \end{cases}$$

We compute the numerical solution until the final time $t = 0.2$ on a uniform mesh with $\Delta x = 1/200$. The solution computed by the mixed-order A-WENO scheme is plotted in Fig. 1. As one can see, there is no oscillations in either velocity or pressure fields at the neighborhood of the contact wave, which demonstrates the robustness of the proposed hybrid approach.

We also measure the relative conservation error in the total energy using formula (3.2). The results reported in Table 1 indicate that while the conservation error decays quite slow when the mesh is refined, it is very small even when the mesh is quite coarse.

**Table 1** Example 1: Conservation error in the total energy computed by (3.2)

| $\Delta x$ | Err | Rate |
|---|---|---|
| 1/200 | 8.35e−4 | – |
| 1/400 | 5.84e−4 | 0.52 |
| 1/800 | 4.58e−4 | 0.35 |
| 1/1600 | 2.70e−4 | 0.76 |
| 1/3200 | 1.62e−4 | 0.74 |
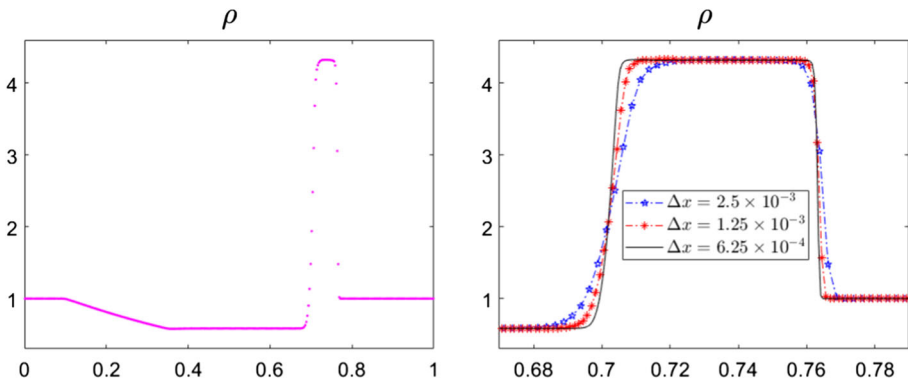


**Fig. 2** Example 2: Density ($\rho$) computed using $\Delta x = 1/400$ (left) and zoomed mesh-refinement study (right)

## Example 2—Stiff Shock-Tube Problem

In the second example, we consider another shock-tube problem with the initial conditions given by

$$(\rho, u, p; \gamma, p_\infty) = \begin{cases} (1, 0, 500; 1.4, 0), & x < 0.5, \\ (1, 0, 0.2; 1.6, 0), & x > 0.5. \end{cases}$$

We compute the solution using the mixed-order A-WENO scheme until the final time $t = 0.015$ on a uniform mesh with $\Delta x = 1/400$ and plot its components in Figs. 2 (density) and 3 (velocity and pressure). As one can observe, the obtained solution is oscillation-free and the achieved resolution is of a high quality. In order to demonstrate the experimental convergence of the proposed scheme, we zoom at the shock and contact wave areas of the density and compute the solution on finer uniform grids with $\Delta x = 1/800$ and $1/1600$. The results of the mesh-refinement study, shown in Fig. 2 (right), indicate a fast and monotone convergence of the solution.

As in the previous example, we measure the conservation error using formula (3.2). As one can observe from the results reported in Table 2, the relative conservation error is still quite small and decays a bit slower than in Example 1 when the mesh is refined.

## Example 3—Water–Air Model Using the Stiff Equation of State

In the last 1-D example, we consider a gas–liquid multifluid system, in which the liquid component is modeled by the stiff EOS (2.4) with $p_{\infty,I} \neq 0$. The initial conditions correspond
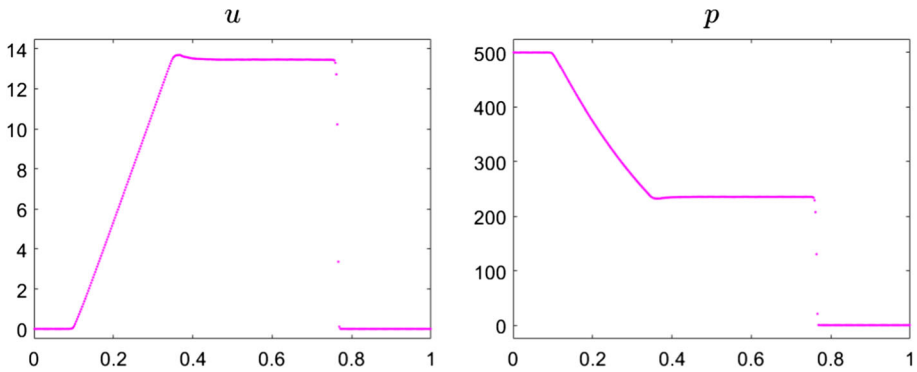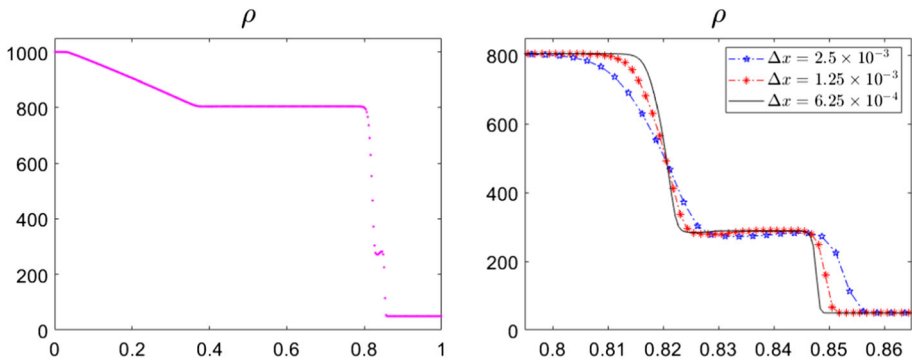
**Fig. 3** Example 2: Velocity ($u$) and pressure ($p$) computed by the mixed-order A-WENO scheme

**Table 2** Example 2: Conservation error in the total energy computed by (3.2)

| $\Delta x$ | Err | Rate |
|---|---|---|
| 1/400 | 1.82e−3 | – |
| 1/800 | 8.12e−4 | 1.16 |
| 1/1600 | 5.27e−4 | 0.62 |
| 1/3200 | 3.74e−4 | 0.49 |
| 1/6400 | 2.50e−4 | 0.58 |



**Fig. 4** Example 3: Density ($\rho$) computed using $\Delta x = 1/400$ (left) and zoomed mesh-refinement study (right)

to a severe water–air shock tube problem and they are given by

$$(\rho, u, p; \gamma, p_\infty) = \begin{cases} (1000, 0, 10^9; 4.4, 6 \cdot 10^8), & x < 0.7, \\ (50, 0, 10^5; 1.4, 0), & x > 0.7. \end{cases}$$

We compute the solution using the mixed-order A-WENO scheme until the final time $t = 0.00025$ on a uniform mesh with $\Delta x = 1/400$ and present the results in Figs. 4 and 5. In order to demonstrate the experimental convergence of the proposed scheme, we perform computations on a series of refined meshes with $\Delta x = 1/800$ and 1/1600, and zoom the solution at the areas of shock and contact waves in Fig. 4 (right). The obtained results clearly indicate that the mixed-order scheme provides a high overall quality of the computed solution.
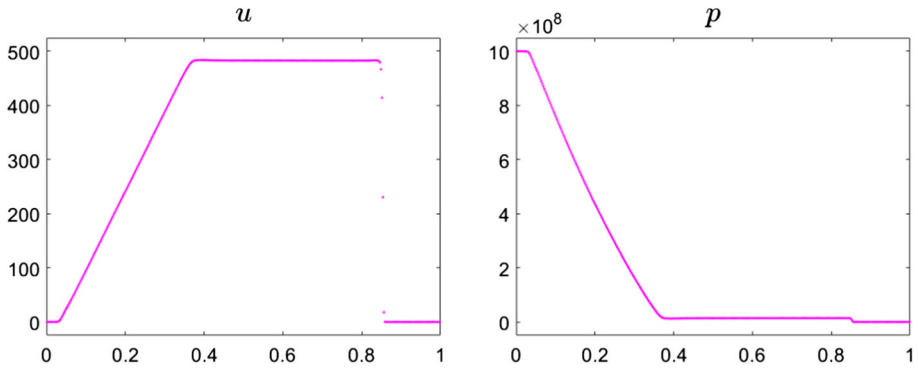
**Fig. 5** Example 3: Velocity ($u$) and pressure ($p$) computed by the mixed-order A-WENO scheme

| | $\Delta x$ | Err | Rate |
|---|---|---|---|
| **Table 3** Example 3: Conservation error in the total energy computed by (3.2) | 1/400 | 5.02e−4 | – |
| | 1/800 | 5.79e−4 | − 0.21 |
| | 1/1600 | 6.19e−4 | − 0.10 |
| | 1/3200 | 3.28e−4 | 0.92 |
| | 1/6400 | 3.29e−4 | − 0.01 |
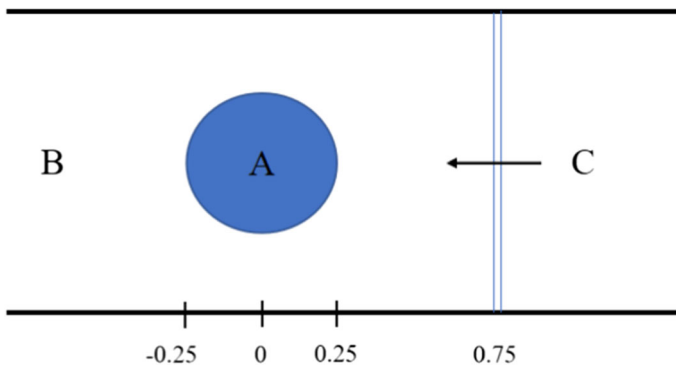


**Fig. 6** Initial setting for the 2-D numerical examples

Once again, we measure the relative conservation error using formula (3.2) and show the results in Table 3. Compared to Examples 1 and 2, the error is slightly larger and it decays extremely slow as mesh is refined. This is due to the large initial jumps in both the density and pressure, which lead to larger conservation error at the initial stages of the solution evolution.

### 3.2 Two-Dimensional Examples

In this section, we use the second-order CU scheme and the mixed-order A-WENO scheme to compute the numerical results of the interaction between a shock and a bubble. A shock wave in the air hits the resting bubble which contains either helium (Example 4) or R22
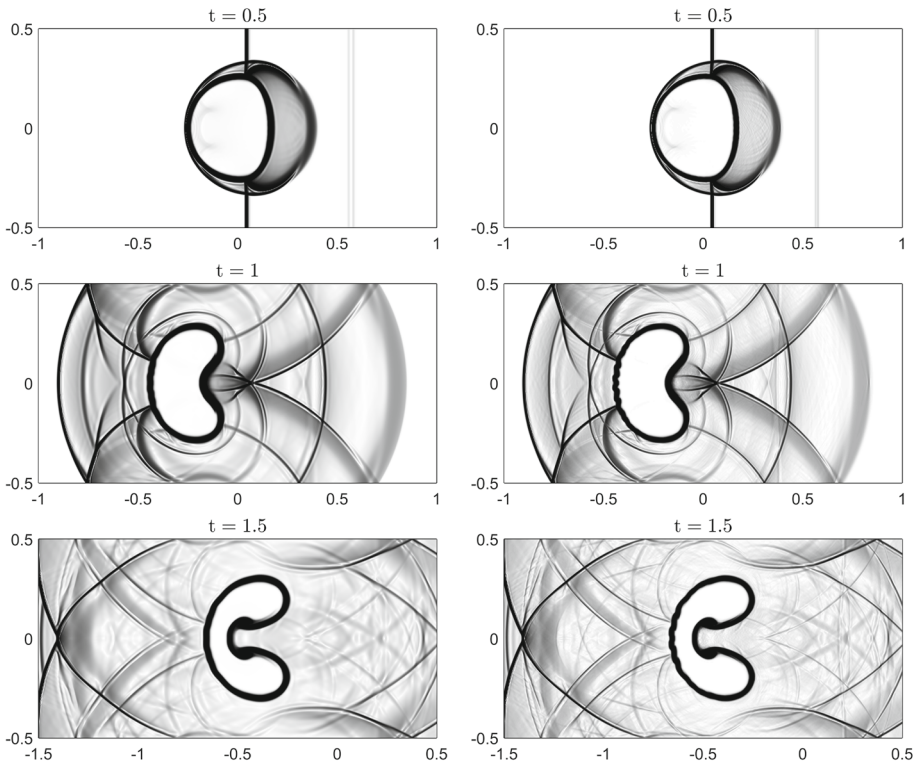
**Fig. 7** Example 4: Shock–helium bubble interaction by the second- (left column) and mixed-order (right column) schemes at times $t = 0.5$, 1 and 1.5

(Example 5). In each case, complicated solution structures are developed having very distinct wave properties since helium is lighter and R22 is heavier than air. These two examples follow the experiments reported in [15] and numerical simulation conducted in [9,33]. The computational domain of the initial setup is shown in Fig. 6. The top and bottom boundaries are solid walls, while the left and right boundaries are open. In both Examples 4 and 5, the uniform spatial grid with $\Delta x = \Delta y = 1/500$ has been used in numerical simulations. In Figs. 7, 8, 9 and 10, we illustrate the results obtained at different time moments during the interaction process. In these figures, we plot Schlieren images of the magnitude of the density gradient field, $|\nabla \rho|$. To this end, we have used the following shading function:

$$\exp\left(-\frac{K|\nabla\rho|}{\max(|\nabla\rho|)}\right), \quad K = 80,$$

where the numerical density derivatives are computed using standard central differencing.
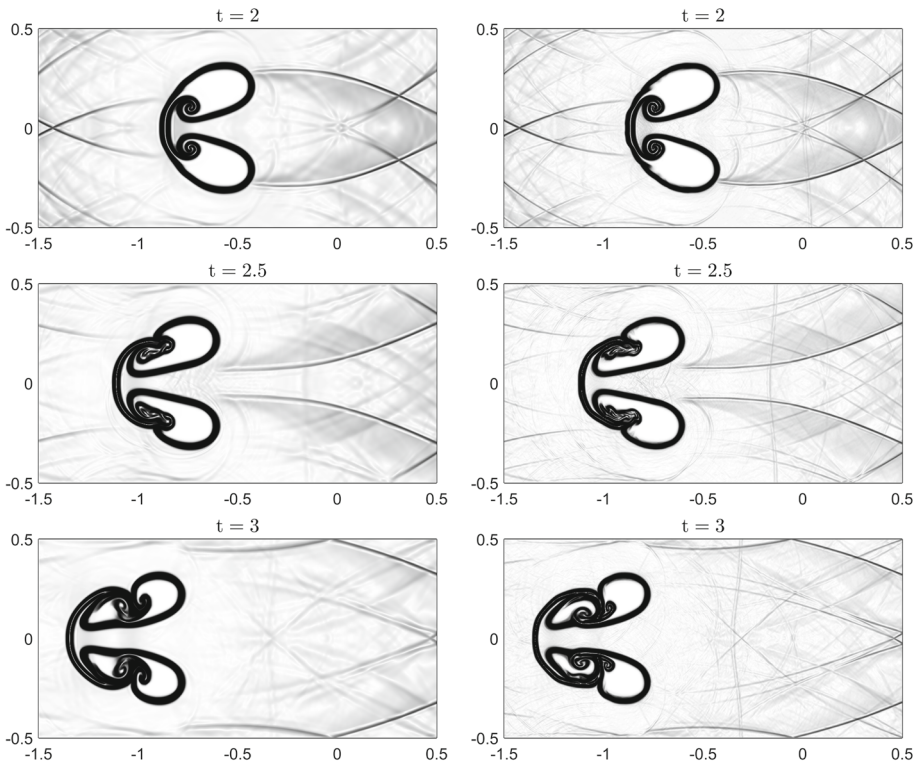
**Fig. 8** Same as in Fig. 7, but at larger times $t = 2, 2.5$ and 3

### Example 4—Helium Bubble

In the first 2-D example, we consider the system (1.1)–(1.5), (1.7) subject to the following initial conditions:

$$(\rho, u, p; \gamma, p_\infty) = \begin{cases} (4/29, 0, 0, 1; 5/3, 0), & \text{in region A,} \\ (1, 0, 0, 1; 1.4, 0), & \text{in region B,} \\ (4/3, -0.3535, 0, 1.5; 1.4, 0), & \text{in region C,} \end{cases}$$

where regions A, B and C are outlined in Fig. 6.

Figures 7 and 8 show different stages of the shock–bubble interaction computed by the second- and mixed-order schemes. When reaching the bubble, the shock wave partially refracts and partially reflects. As the speed of sound in helium is faster than that in air, the refracted shock is curved and propagates inside the helium bubble faster than in the air. Under the force of the shock, the bubble compresses and is put into motion. The helium accelerates more under the influence of the shock and a shear layer is created through the bubble interface, giving rise to highly complex refraction patterns. After the shock finishes its sweep over the bubble, the bubble begins to grow slowly into a recognizable kidney shape until losing its integrity and breaking up. The obtained results are in good agreement with the numerical results reported in [9,33]. From Figs. 7 and 8, one can see that the mixed-order A-WENO scheme can capture the material interface sharper and resolve more small
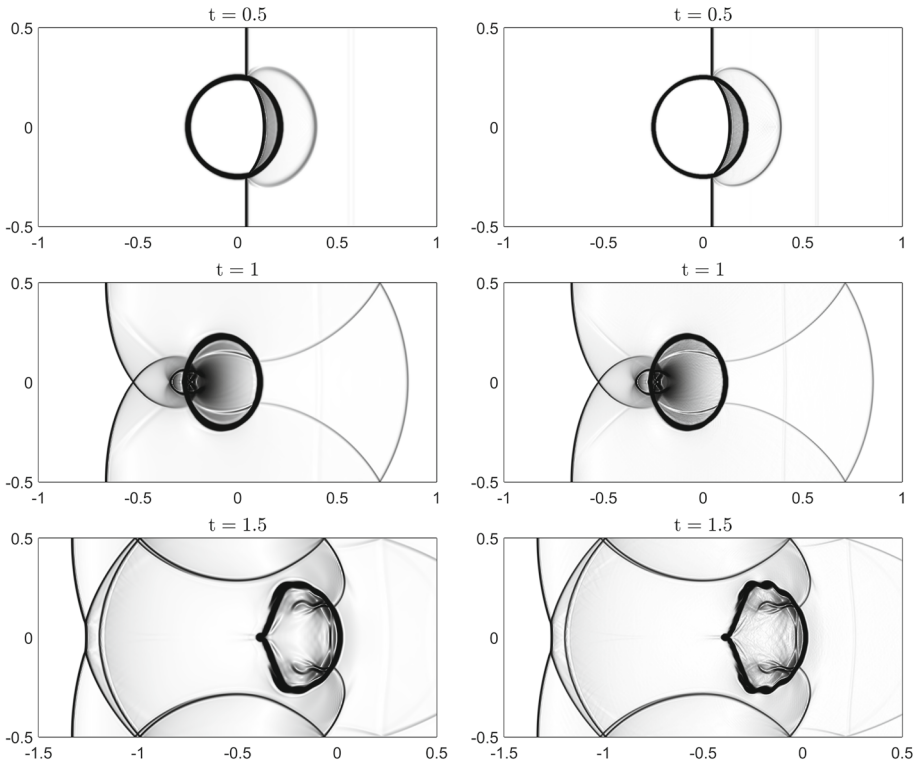
**Fig. 9** Example 5: Shock–R22 bubble interaction by the second- (left column) and mixed-order (right column) schemes at times $t = 0.5$, 1 and 1.5

details of the solution than the second-order scheme, especially near the interface at large computational times; see Fig. 8.

### Example 5—R22 Bubble

In the second 2-D example, we consider the following initial conditions:

$$(\rho, u, p; \gamma, p_\infty) = \begin{cases} (3.1538, 0, 0, 1; 1.249, 0), & \text{in region A,} \\ (1, 0, 0, 1; 1.4, 0), & \text{in region B,} \\ (4/3, -0.3535, 0, 1.5; 1.4, 0), & \text{in region C,} \end{cases}$$

where, as in the previous example, the regions A, B and C are specified in Fig. 6.
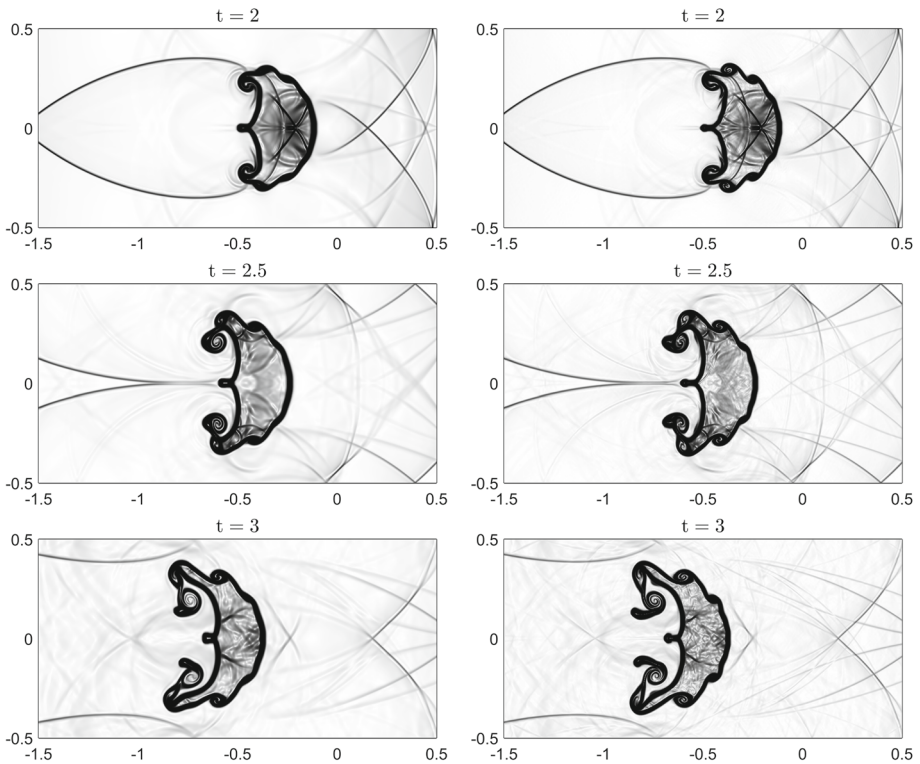
**Fig. 10** Same as in Fig. 9, but at larger times $t = 2$, 2.5 and 3

In Figs. 9 and 10, we present different stages of the shock–bubble interaction computed by the second- and mixed-order schemes. The R22 heavy bubble compresses and undergoes a deformation upon being hit by the shock wave, and the shock partly reflects and partly refracts. Unlike the case of a light helium bubble studied in Example 4, the speed of sound inside the R22 bubble is lower than the outside speed, allowing the refracted shock wave to travel more slowly than the shock outside the bubble. As the bubble is heavier than the surrounding air, it accelerates less than the air under the influence of the shock. As a consequence, vorticity is created at the bubble interface. It is possible to observe that the refracted shock concentrates inside the bubble, creating a pressure increase and resulting in a noticeable forward jet around the middle of the bubble. If the shear begins to develop under the induced vorticity field, the shear at the boundary interface allows the interface to roll up. The obtained results are in good agreement with the results reported in [9,33]. From Figs. 9 and 10 one can see that, as in Example 4, the mixed-order A-WENO scheme can capture both the material interface and small futures of the solution in a sharper manner than its second-order counterpart. The difference in the results computed by the two studied schemes becomes larger at larger times; see Fig. 10.

## Declarations

**Conflict of interest** On behalf of all authors, the corresponding author states that there is no conflict of interest.

## Appendix: Semi-discrete Central-Upwind (CU) Scheme

In this section, we briefly describe the semi-discrete CU scheme for the homogeneous 2-D systems (1.1)–(1.5). The 2-D semi-discrete CU scheme from [8,21] admits the following flux form:

$$\frac{d}{dt}\overline{U}_{j,k} = -\frac{H^x_{j+\frac{1}{2},k} - H^x_{j-\frac{1}{2},k}}{\Delta x} - \frac{H^y_{j,k+\frac{1}{2}} - H^y_{j,k-\frac{1}{2}}}{\Delta y},$$

where the numerical fluxes are

$$H^x_{j+\frac{1}{2},k} = \frac{a^+_{j+\frac{1}{2},k}F(U^E_{j,k}) - a^-_{j+\frac{1}{2},k}F(U^W_{j+1,k})}{a^+_{j+\frac{1}{2},k} - a^-_{j+\frac{1}{2},k}} + a^+_{j+\frac{1}{2},k}a^-_{j+\frac{1}{2},k}$$

$$\times \left[\frac{U^W_{j+1,k} - U^E_{j,k}}{a^+_{j+\frac{1}{2},k} - a^-_{j+\frac{1}{2},k}} - Q^x_{j+\frac{1}{2},k}\right],$$

$$H^y_{j,k+\frac{1}{2}} = \frac{b^+_{j,k+\frac{1}{2}}G(U^N_{j,k}) - b^-_{j,k+\frac{1}{2}}G(U^S_{j,k+1})}{b^+_{j,k+\frac{1}{2}} - b^-_{j,k+\frac{1}{2}}} + b^+_{j,k+\frac{1}{2}}b^-_{j,k+\frac{1}{2}}$$

$$\times \left[\frac{U^N_{j,k+1} - U^S_{j,k}}{b^+_{j,k+\frac{1}{2}} - b^-_{j,k+\frac{1}{2}}} - Q^y_{j,k+\frac{1}{2}}\right]. \tag{A.1}$$

Here, $U^E, U^W, U^N, U^S$ are the approximate point values of $U$, which are computed as follows. First, from the available cell averages $\overline{U}_{j,k} = \left(\overline{\rho}_{j,k}, (\overline{\rho u})_{j,k}, (\overline{\rho v})_{j,k}, \overline{E}_{j,k}, (\overline{\rho\phi})_{j,k}\right)^\top$, we compute cell centered values of the velocities $u$ and $v$ and pressure $p$:

$$u_{j,k} = \frac{(\overline{\rho u})_{j,k}}{\overline{\rho}_{j,k}}, \quad v_{j,k} = \frac{(\overline{\rho v})_{j,k}}{\overline{\rho}_{j,k}},$$

$$p_{j,k} = (\gamma_{j,k} - 1)\left[\overline{E}_{j,k} - \frac{\left((\overline{\rho u})_{j,k}\right)^2 + \left((\overline{\rho v})_{j,k}\right)^2}{2\overline{\rho}_{j,k}}\right] - \gamma_{j,k}(p_\infty)_{j,k}, \tag{A.2}$$

and construct a piecewise linear reconstruction applied to the primitive variables $V = (\rho, u, v, p, \phi)^\top$:

$$\widetilde{V}(x, y) = \overline{V}_{j,k} + (V_x)_{j,k}(x - x_j) + (V_y)_{j,k}(y - y_k), \quad (x, y) \in C_{j,k}.$$

We then obtain

$$V^E_{j,k} = \overline{V}_{j,k} + \frac{\Delta x}{2}(V_x)_{j,k}, \quad V^W_{j,k} = \overline{V}_{j,k} - \frac{\Delta x}{2}(V_x)_{j,k},$$

$$V^N_{j,k} = \overline{V}_{j,k} + \frac{\Delta y}{2}(V_y)_{j,k}, \quad V^S_{j,k} = \overline{V}_{j,k} - \frac{\Delta y}{2}(V_y)_{j,k}, \tag{A.3}$$

which are the values of $\widetilde{V}$ at midpoints of the edges of the cell $C_{j,k}$. As in the 1-D case, the numerical derivatives $(V_x)_{j,k}$ and $(V_y)_{j,k}$ are computed using the generalized minmod limiter as

$$(V_x)_{j,k} = \text{minmod}\left(\theta \frac{\overline{V}_{j+1,k} - \overline{V}_{j,k}}{\Delta x}, \frac{\overline{V}_{j+1,k} - \overline{V}_{j-1,k}}{2\Delta x}, \theta \frac{\overline{V}_{j,k} - \overline{V}_{j-1,k}}{\Delta x}\right),$$

$$(V_y)_{j,k} = \text{minmod}\left(\theta \frac{\overline{V}_{j,k+1} - \overline{V}_{j,k}}{\Delta y}, \frac{\overline{V}_{j,k+1} - \overline{V}_{j,k-1}}{2\Delta y}, \theta \frac{\overline{V}_{j,k} - \overline{V}_{j,k-1}}{\Delta y}\right),$$

where the minmod function is defined by (2.13) and, as in the 1-D case, applied to the vector quantity $V$ in a component-wise manner.

The built-in "anti-diffusion" terms $Q^x_{j+\frac{1}{2},k}$ and $Q^y_{j,k+\frac{1}{2}}$ in (A.1) are given by (see [8])

$$Q^x_{j+\frac{1}{2},k} = \text{minmod}\left(\frac{U^*_{j+\frac{1}{2},k} - U^E_{j,k}}{a^+_{j+\frac{1}{2},k} - a^-_{j+\frac{1}{2},k}}, \frac{U^W_{j+1,k} - U^*_{j+\frac{1}{2},k}}{a^+_{j+\frac{1}{2},k} - a^-_{j+\frac{1}{2},k}}\right),$$

$$Q^y_{j,k+\frac{1}{2}} = \text{minmod}\left(\frac{U^*_{j,k+\frac{1}{2}} - U^N_{j,k}}{b^+_{j,k+\frac{1}{2}} - b^-_{j,k+\frac{1}{2}}}, \frac{U^S_{j,k+1} - U^*_{j,k+\frac{1}{2}}}{b^+_{j,k+\frac{1}{2}} - b^-_{j,k+\frac{1}{2}}}\right),$$

where

$$U^*_{j+\frac{1}{2},k} = \frac{a^+_{j+\frac{1}{2},k} U^W_{j+1,k} - a^-_{j+\frac{1}{2},k} U^E_{j,k} - \left\{F(U^W_{j+1,k}) - F(U^E_{j,k})\right\}}{a^+_{j+\frac{1}{2},k} - a^-_{j+\frac{1}{2},k}},$$

$$U^*_{j,k+\frac{1}{2}} = \frac{b^+_{j,k+\frac{1}{2}} U^S_{j,k+1} - b^-_{j,k+\frac{1}{2}} U^N_{j,k} - \left\{G(U^S_{j,k+1}) - G(U^N_{j,k})\right\}}{b^+_{j,k+\frac{1}{2}} - b^-_{j,k+\frac{1}{2}}}.$$

Finally, $a^\pm_{j+\frac{1}{2},k}$ and $b^\pm_{j,k+\frac{1}{2}}$ are the one-sided local propagation speeds in the $x$- and $y$-directions, respectively. They are obtained using the largest/smallest eigenvalues of the Jacobians $\frac{\partial F}{\partial U}$ and $\frac{\partial G}{\partial U}$. For the reactive Euler systems (1.1)–(1.5), these speeds can be estimated by

$$a^+_{j+\frac{1}{2},k} = \max\left(u^E_{j,k} + c^E_{j,k}, u^W_{j+1,k} + c^W_{j+1,k}, 0\right),$$

$$a^-_{j+\frac{1}{2},k} = \min\left(u^E_{j,k} - c^E_{j,k}, u^W_{j+1,k} - c^W_{j+1,k}, 0\right),$$

$$b^+_{j,k+\frac{1}{2}} = \max\left(u^N_{j,k} + c^N_{j,k}, u^S_{j,k+1} + c^S_{j,k+1}, 0\right),$$

$$b^-_{j,k+\frac{1}{2}} = \min\left(u^N_{j,k} - c^N_{j,k}, u^S_{j,k+1} - c^S_{j,k+1}, 0\right),$$

where $c = \sqrt{\gamma(p + p_\infty)/\rho}$.

# References

1. Abgrall, R., Karni, S.: Computations of compressible multifluids. J. Comput. Phys. **169**, 594–623 (2001)
2. Abgrall, R., Karni, S.: Ghost-fluids for the poor: a single fluid algorithm for multifluids. In: Hyperbolic Problems: Theory, Numerics, Applications. Birkhäuser, Basel (2001)

3. Abgrall, R., Saurel, R.: Discrete equations for physical and numerical compressible multiphase mixtures. J. Comput. Phys. **186**, 361–396 (2003)
4. Allaire, G., Clerc, S., Kokh, S.: A five-equation model for the simulation of interfaces between compressible fluids. J. Comput. Phys. **181**, 577–616 (2002)
5. Baer, M.R., Nunziato, J.W.: A two-phase mixture theory for the deflagration-to-detonation transition (ddt) in reactive granular materials. Int. J. Multiphas. Flow **12**, 861–889 (1986)
6. Castro Díaz, M. J., Kurganov, A., Morales de Luna, T.: Path-conservative central-upwind schemes for nonconservative hyperbolic systems. ESAIM Math. Model. Numer. Anal. **53**, 959–985 (2019)
7. Cheng, J., Zhang, F., Liu, T.G.: A quasi-conservative discontinuous Galerkin method for solving five equation model of compressible two-medium flows. J. Sci. Comput. **85**, 12–35 (2020)
8. Chertock, A., Cui, S.M., Kurganov, A., Özcan, C.N., Admor, E.T.: Well-balanced schemes for the Euler equations with gravitation: conservative formulation using global fluxes. J. Comput. Phys. **358**, 36–52 (2018)
9. Chertock, A., Karni, S., Kurganov, A.: Interface tracking method for compressible multifluids. M2AN Math. Model. Numer. Anal. **42**, 991–1019 (2008)
10. Chu, S., Kurganov, A., Na, M.Y.: Fifth-order a-weno finite-difference schemes based on the path-conservative central-upwind method (in preparation)
11. Don, W.S., Li, D.-M., Gao, Z., Wang, B.-S.: A characteristic-wise alternative WENO-Z finite difference scheme for solving the compressible multicomponent non-reactive flows in the overestimated quasi-conservative form. J. Sci. Comput. **82**, 24 (2020)
12. Fedkiw, R.P., Aslam, T., Merriman, B., Osher, S.: A non-oscillatory Eulerian approach to interfaces in multimaterial flows (the ghost fluid method). J. Comput. Phys. **152**, 457–492 (1999)
13. Gottlieb, S., Ketcheson, D., Shu, C.-W.: Strong Stability Preserving Runge–Kutta and Multistep Time Discretizations. World Scientific Publishing Co World Scientific, Hackensack (2011)
14. Gottlieb, S., Shu, C.-W., Tadmor, E.: Strong stability-preserving high-order time discretization methods. SIAM Rev. **43**, 89–112 (2001)
15. Haas, J.-F., Sturtevant, B.: Interaction of weak shock waves with cylindrical and spherical gas inhomogeneities. J. Fluid Mech. **181**, 41–76 (1987)
16. He, Z.W., Li, L., Zhang, Y.S., Tian, B.L.: Consistent implementation of characteristic flux-split based finite difference method for compressible multi-material gas flows. Comput. Fluids **168**, 190–200 (2018)
17. Hesthaven, J.S.: Numerical Methods for Conservation Laws, vol. 18 of Computational Science and Engineering. Society for Industrial and Applied Mathematics (SIAM), Philadelphia, PA (2018)
18. Jiang, Y., Shu, C.-W., Zhang, M.P.: An alternative formulation of finite difference weighted ENO schemes with Lax–Wendroff time discretization for conservation laws. SIAM J. Sci. Comput. **35**, A1137–A1160 (2013)
19. Johnsen, E., Colonius, T.: Implementation of WENO schemes in compressible multicomponent flow problems. J. Comput. Phys. **219**, 715–732 (2006)
20. Karni, S.: Hybrid multifluid algorithms. SIAM J. Sci. Comput. **17**, 1019–1039 (1996)
21. Kurganov, A., Lin, C.-T.: On the reduction of numerical dissipation in central-upwind schemes. Commun. Comput. Phys. **2**, 141–163 (2007)
22. Kurganov, A., Noelle, S., Petrova, G.: Semidiscrete central-upwind schemes for hyperbolic conservation laws and Hamilton–Jacobi equations. SIAM J. Sci. Comput. **23**, 707–740 (2001)
23. Lei, X., Du, Z., Li, J.: The simulation of compressible multi-fluid flows by a GRP-based energy-splitting method. Comput. Fluids **181**, 416–428 (2019)
24. Lei, X., Li, J.: An energy-splitting high order numerical method for multi-material flows. arXiv:2010.01515 (2020)
25. LeVeque, R.J.: Finite Volume Methods for Hyperbolic Problems, Cambridge Texts in Applied Mathematics. Cambridge University Press, Cambridge (2002)
26. Lie, K.-A., Noelle, S.: On the artificial compression method for second-order nonoscillatory central difference schemes for systems of conservation laws. SIAM J. Sci. Comput. **24**, 1157–1174 (2003)
27. Liu, H.: A numerical study of the performance of alternative weighted ENO methods based on various numerical fluxes for conservation law. Appl. Math. Comput. **296**, 182–197 (2017)
28. Liu, H., Qiu, J.: Finite difference Hermite WENO schemes for conservation laws, II: an alternative approach. J. Sci. Comput. **66**, 598–624 (2016)
29. Mulder, W., Osher, S., Sethian, J.A.: Computing interface motion in compressible gas dynamics. J. Comput. Phys. **100**, 209–228 (1992)
30. Nessyahu, H., Tadmor, E.: Nonoscillatory central differencing for hyperbolic conservation laws. J. Comput. Phys. **87**, 408–463 (1990)

31. Nonomura, T., Fujii, K.: Characteristic finite-difference WENO scheme for multicomponent compressible fluid analysis: overestimated quasi-conservative formulation maintaining equilibriums of velocity, pressure, and temperature. J. Comput. Phys. **340**, 358–388 (2017)
32. Nonomura, T., Morizawa, S., Terashima, H., Obayashi, S., Fujii, K.: Numerical (error) issues on compressible multicomponent flows using a high-order differencing scheme: weighted compact nonlinear scheme. J. Comput. Phys. **231**, 3181–3210 (2012)
33. Quirk, J., Karni, S.: On the dynamics of a shock–bubble interaction. J. Fluid Mech. **318**, 129–163 (1996)
34. Saurel, R., Abgrall, R.: A multiphase Godunov method for compressible multifluid and multiphase flows. J. Comput. Phys. **150**, 425–467 (1999)
35. Saurel, R., Abgrall, R.: A simple method for compressible multifluid flows. SIAM J. Sci. Comput. **21**, 1115–1145 (1999)
36. Shyue, K.M.: An efficient shock-capturing algorithm for compressible multicomponent problems. J. Comput. Phys. **142**, 208–242 (1998)
37. Sweby, P.K.: High resolution schemes using flux limiters for hyperbolic conservation laws. SIAM J. Numer. Anal. **21**, 995–1011 (1984)
38. Toro, E.F.: Riemann Solvers and Numerical Methods for Fluid Dynamics: A Practical Introduction, 3rd edn. Springer, Berlin, Heidelberg (2009)
39. Wang, B.-S., Don, W.S., Garg, N.K., Kurganov, A.: Fifth-order A-WENO finite-difference schemes based on a new adaptive diffusion central numerical flux. SIAM J. Sci. Comput. **42**, A3932–A3956 (2020)
40. Wang, B.-S., Li, P., Gao, Z., Don, W.S.: An improved fifth order alternative WENO-Z finite difference scheme for hyperbolic conservation laws. J. Comput. Phys. **374**, 469–477 (2018)
41. Wang, C.W., Shu, C.-W.: An interface treating technique for compressible multi-medium flow with Runge–Kutta discontinuous Galerkin method. J. Comput. Phys. **229**, 8823–8843 (2010)